

Geophysical Research Letters[®]

RESEARCH LETTER

10.1029/2022GL098977

Key Points:

- Interferometric Synthetic Aperture Radar (InSAR) & Global Navigation Satellite System (GNSS) velocities indicate ~19 mm/yr widening across a dike after its formation interpreted as post-rifting viscoelastic relaxation
- A two-layer viscoelastic model with 0.4×10^{19} Pa s viscoelastic half-space below 18 km depth best explains the GNSS and InSAR observations
- Elastic thickness of ~18 km provides best fit, but a comparable fit is at ~2 km, most likely due to unmodeled processes

Supporting Information:

Supporting Information may be found in the online version of this article.

Correspondence to:

S. Li,
sil10@hi.is






Citation:

Li, S., Grapenthin, R., Sigmundsson, F., Drouin, V., Hreinsdóttir, S., & Ófeigsson, B. G. (2022). Post-rifting relaxation during 2015–2020 following the Bárðarbunga-Holuhraun dike intrusion and eruption in Iceland. *Geophysical Research Letters*, 49, e2022GL098977. <https://doi.org/10.1029/2022GL098977>

Received 8 APR 2022

Accepted 20 JUN 2022

Post-Rifting Relaxation During 2015–2020 Following the Bárðarbunga-Holuhraun Dike Intrusion and Eruption in Iceland

Siqi Li¹ , Ronni Grapenthin² , Freysteinn Sigmundsson¹ , Vincent Drouin³ ,
Sigrún Hreinsdóttir⁴ , and Benedikt G. Ófeigsson³

¹Nordic Volcanological Center, Institute of Earth Sciences, University of Iceland, Reykjavík, Iceland, ²Geophysical Institute, Department of Geosciences, University of Alaska Fairbanks, Fairbanks, AK, USA, ³Icelandic Meteorological Office, Reykjavík, Iceland, ⁴GNS Science, Lower Hutt, New Zealand

Abstract Post-rifting ground deformation may be driven by viscoelastic relaxation of stresses generated by dike intrusions. The single-dike intrusion of the 2014–2015 Bárðarbunga eruption in Iceland presents an opportunity for a detailed study of this process. We use continuous Global Navigation Satellite System (GNSS) and Interferometric Synthetic Aperture Radar (InSAR) velocity fields to analyze the 2015–2020 post-rifting deformation, showing uplift on both sides of the dike and horizontal displacement away from the dike after correcting for background deformation. Two GNSS stations experience baseline lengthening at a rate of 19 mm/yr in the direction perpendicular to the strike of the dike. A two-layer viscoelastic model with a 0.4×10^{19} Pa s viscoelastic half-space overlain by an 18 km thick elastic layer best explains the observed horizontal and vertical InSAR and GNSS displacements. The model misfit space shows a second regime of good fit, likely driven by deformation near the dike that may result from cooling compaction of the emplaced dike.

Plain Language Summary Surface displacement can continue for years after a fissure eruption ends. This has been found at some volcanoes, such as in Afar (Ethiopia) and Krafla (Iceland). The 2014–2015 Bárðarbunga eruption in Iceland created a 48 km long dike, that led to an eruption to the northeast of the Bárðarbunga caldera outside the Vatnajökull ice cap. Here, we focus on exploring an explanation for the surface movement in the dike area after the eruption. Other non-volcanic processes cause surface movements in the area, including glacial isostatic adjustment caused by the ice retreat and plate spreading due to the divergence of the Eurasian plate and North American plate. We first correct for deformation due to these processes. The remaining deformation signal shows uplift on both sides of the dike and horizontal displacement away from the dike. We test if a two-layer model consisting of an elastic layer on top of a viscoelastic half-space can explain our observations. Our results suggest that material properties similar to other nearby areas explain the observations well. Systematic difference between observed and modeled deformation near the dike feeding the eruption is likely due to its cooling.

1. Introduction

The Bárðarbunga volcanic system is located in central Iceland at the divergent plate boundary between the North American and Eurasian plates, with a caldera, central volcano, and part of its fissure swarm lying under the Vatnajökull ice cap (Figure 1). In August 2014, a dike propagated away from the caldera, leading to a 6-month-long Holuhraun eruption at the far end of the dike until February 2015, which resulted in a collapse of the Bárðarbunga caldera (Gudmundsson et al., 2016; Pedersen et al., 2017). The track of the 48 km long segmented dike was well constrained by the analysis of seismicity and deformation data (e.g., Ágústsson et al., 2016, 2019; Sigmundsson et al., 2015; Woods et al., 2018). Observations at two continuous Global Navigation Satellite System (GNSS) stations, located 25 km apart on each side of the dike, recorded 1.3 m lengthening between the stations during the activity (Sigmundsson et al., 2015).

Excessive surface displacement has been observed following the 2014–2015 Bárðarbunga-Holuhraun eruption. Li et al. (2021) infer that the post-rifting deformation to the northwest of the Bárðarbunga caldera may be caused by either post-eruption inflation, viscoelastic relaxation in response to magma withdrawal from beneath the caldera, or a combination of both processes. They considered a two-layer rheological crustal structure: a 7 km thick elastic layer on top of a viscoelastic halfspace (Maxwell rheology). If the viscoelastic relaxation process is

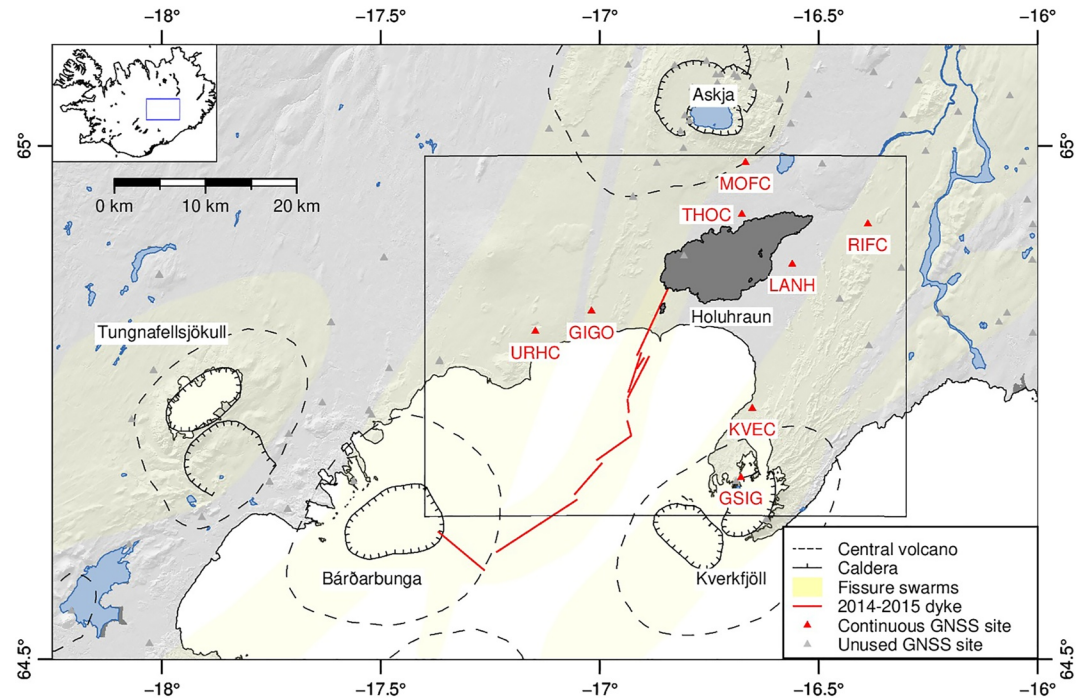


Figure 1. Map view of the Bárðarbunga central volcano, the Bárðarbunga-Holuhraun dike, and surroundings (red lines showing dike segments inferred by Sigmundsson et al. (2015)). The rectangle area marked with black boundary is our study area. The Holuhraun lava field is shown in dark gray. Yellow transparent layers show locations of fissure swarms (for geological layers, see Sigmundsson et al. (2020) and references therein). Glaciers are shown in white. Red triangles are continuous Global Navigation Satellite System (GNSS) sites used in this study. Gray triangles show GNSS stations not used.

the only explanation, the viscosity that best explains the observations is 0.3×10^{19} Pa s assuming a shear modulus of 30 GPa.

As our study area is adjacent to the Vatnajökull ice cap, studies of glacial isostatic adjustment (GIA) can provide important information on the subsurface viscoelastic properties. GIA studies in Iceland have mainly used GNSS data (Árnadóttir et al., 2009; Fleming et al., 2007; Pagli et al., 2007), sometimes in combination with other techniques, such as Interferometric Synthetic Aperture Radar (InSAR; Auriac, 2014), and gravity (Jacoby et al., 2009). These studies find models with a 10–40 km thick uppermost elastic layer, underlain by viscoelastic material with a viscosity in the range of 0.01 – 1×10^{19} Pa s.

Several studies have addressed viscoelastic relaxation in response to emplacement of large dikes during rifting episodes, such as the 1978 Ghoubbet-Asal rifting episode in Djibouti, Africa (Cattin et al., 2005), the Dabbahu 2005–2010 rifting episode in Afar (Hamling et al., 2014; Nooner et al., 2009; Wright et al., 2012), and the 1975–1984 Krafla rifting episode in north Iceland (Ali et al., 2014; Foulger et al., 1992; Pollitz & Sacks, 1996). For the Ghoubbet-Asal seismovolcanic crisis, Cattin et al. (2005) suggest dike inflation and fault creep as the main sources for post-rifting deformation, although part of the rifting could be the result of viscoelastic relaxation. The Dabbahu rifting episode consisted of 14 dike intrusions. Viscoelastic modeling indicates a 12–30 km thick elastic layer on top of a viscoelastic material with a viscosity of 0.1 – 1×10^{19} Pa s (Hamling et al., 2014; Nooner et al., 2009). The Krafla rifting episode includes around 20 diking events, nine of them ending in an eruption. Modeling of deformation data, spanning more than 20 years in the post-eruptive period, is consistent with deformation driven by the viscoelastic response to diking events (e.g., Foulger et al., 1992; Pollitz & Sacks, 1996). The most recent study suggests an elastic layer thickness of 8.0–9.5 km for the Krafla region, underlain by viscoelastic lower crust with a viscosity in the range of 1.9 – 4.9×10^{19} Pa s (Ali et al., 2014).

We analyze and model the post-rifting deformation associated with the 2014–2015 Bárðarbunga-Holuhraun dike. Given the dike volume of about 0.6 km^3 with an average opening of 1.0 m (Gudmundsson et al., 2016; Parks et al., 2017), we expect appreciable post-rifting relaxation as previously observed from the events referenced

above. We analyze InSAR and GNSS data to examine ground deformation. We limit our study area (Figure 1) to a region where the influence of the post-eruptive deformation around the Bárðarbunga caldera and the long-term subsidence at Askja volcano (see location in Figure 1) are not significant. Our study period is selected to be the relatively quiet period from March 2015 to December 2020, after the cessation of the 2014–2015 Bárðarbunga eruption and before the onset of measurable Askja inflation in August 2021. We consider a two-layer viscoelastic model for post-rifting relaxation surface displacement. By varying the thickness of the top elastic layer and the viscosity of the lower viscoelastic half-space, we explore if such a rheological model explains our observations. The Bárðarbunga rifting event overlaps with GIA processes, which allows us to sample the rheologic properties at different spatial and temporal periods. Importantly, this rifting event involves only one dike intrusion, which provides us the opportunity to better understand the role of viscoelastic relaxation in the post-rifting deformation field, and guides future studies of post-rifting deformation in general.

2. Observations

2.1. GNSS

We use data from 8 continuous GNSS stations north of the Vatnajökull ice cap, on both sides of the dike (Figure 1). The data are analyzed with the GAMIT/GLOBK 10.7 software (Herring et al., 2010; Hreinsdóttir et al., 2009) in the ITRF2014 (Altamimi et al., 2016) reference frame. We present our solutions relative to the stable Eurasian plate (Argus et al., 2010). Daily site positions are derived from the data to form timeseries of three-dimensional displacements.

We estimate seasonal variations in each displacement component using the equation

$$disp = A\cos(\omega t) + B\sin(\omega t) + C\cos(\omega 2t) + D\sin(\omega 2t) + vt \quad (1)$$

modified from Grapenthin et al. (2006), where t represents the time over which the station data are observed, v represents the estimated average velocity, and $disp$ is a vector containing the observed east, north, and up GNSS timeseries. The angular frequency ω is $\frac{2\pi}{365}$ to span the period of 1 year. We estimate annual and semiannual coefficients A , B , C , D for the three displacement directions separately through least squares inversion. These estimates of seasonal variations are then removed from the observed GNSS timeseries (Figures S1–S8 in Supporting Information S1).

We correct the timeseries for the background deformation processes, including plate spreading and GIA caused by ice retreat, which also causes ground deformation in our study area. GIA generates surface uplift and displacement toward the north, as suggested by the model from Auriac (2014). Li et al. (2021) applied a scaling factor to the GIA model from Auriac (2014) to correct for the GIA displacement during the period 2015–2018. We assume the GIA signal does not change from 2015 to 2020 and apply the same scaling factor to correct for the GIA signal as done by Li et al. (2021). Plate spreading in our study area is caused by the divergent plate movements as the Eurasian and North American plates move apart. The divergent plate boundary is striking in an approximately north-south direction in our area. We apply the plate spreading model by Drouin and Sigmundsson (2019) to remove this signal.

The average velocities in the north, east, and up components are estimated using a linear inverse function, which are referred to as corrected velocity in the following text. The GIGO and KVEC stations (Figure 1) are closest to the dike on each side of it, spaced about 20 km apart, 6 and 13 km from the dike, respectively. Their horizontal velocities can be rotated into velocity components parallel and perpendicular to the dike, yielding 9.0 mm/yr and 10.2 mm/yr dike-perpendicular average velocities at GIGO and KVEC, respectively (Figure 2). The vertical velocity at GIGO is 9.3 mm/yr, similar to 8.5 mm/yr estimated at KVEC.

KVEC shows a temporal variation in the horizontal component from 2015 to 2020 (Figures 2 and S3 in Supporting Information S1). If this temporal variation of surface displacement were caused by viscoelastic relaxation, we would expect exponential decay of the displacement. Therefore, we also fit the following equation to the observed displacement:

$$disp = Ae^{-\frac{1}{\tau}t} \quad (2)$$

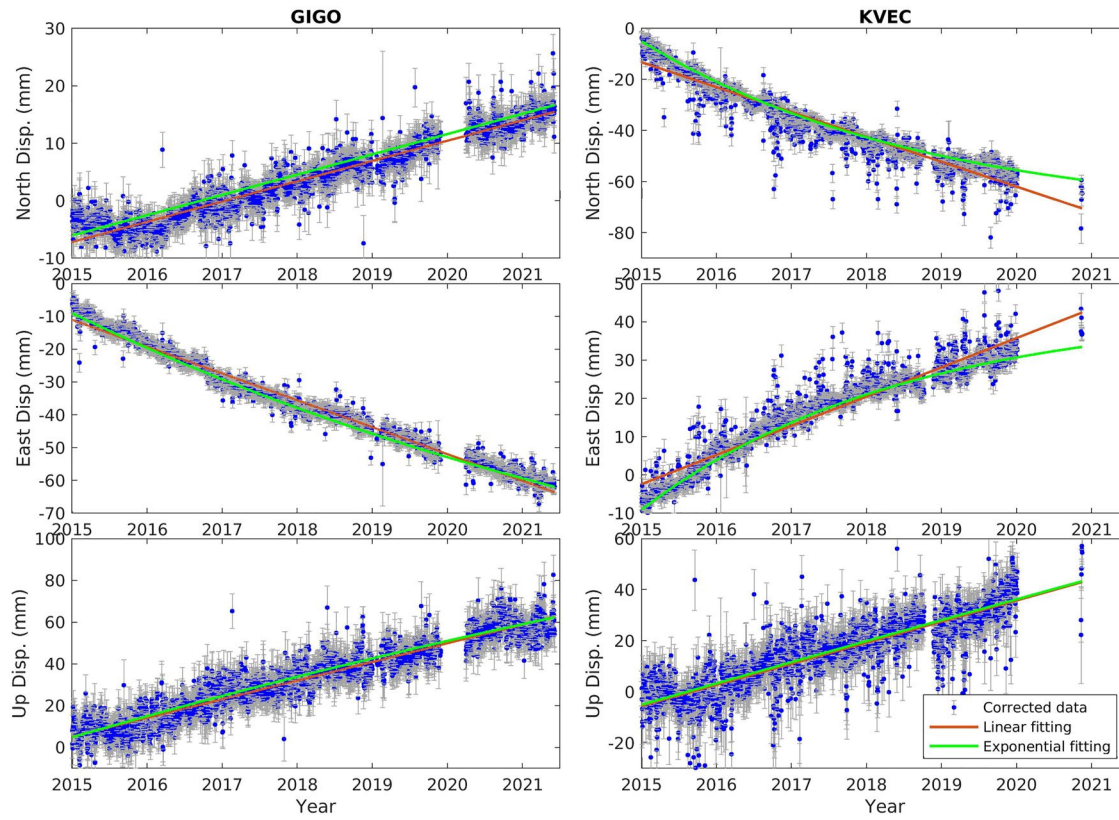


Figure 2. Corrected Global Navigation Satellite System timeseries at GIGO (left) and KVEC (right) stations. Timeseries are referenced to the Eurasian plate and then corrected for seasonal variation (annual and semi-annual cycle), glacial isostatic adjustment, and plate spreading (see the data before correction in Figures S1–S8 in Supporting Information S1). The timeseries are then both fit for linear displacement (red) and exponential decay (green). From top to bottom, the panels show north, east, and up displacements in mm.

where t is the time in years and $disp$ is the displacement over time. A and T are the amplitude of the displacement and the relaxation time. For KVEC, we find a relaxation time of 3 years in the horizontal direction. Station GIGO also shows a smaller temporal variation, with a relaxation time of 10 years. Both stations show almost insignificant temporal variation in the vertical direction. The same analysis is carried out for all the GNSS stations (Table S1 in Supporting Information S1). The majority of the stations show a slight temporal variation in the horizontal direction, but none of them show significant temporal variation in the vertical (Figures S1–S8 in Supporting Information S1).

2.2. InSAR

We analyze SAR data collected from Sentinel-1 satellites every June–October 2015–2020 using the InSAR Scientific Computing Environment (ISCE) software (Rosen et al., 2012). Average line-of-sight (LOS) velocity fields are produced using the small baseline method. The average LOS velocities from Track 9 (descending), 111 (descending), and 147 (ascending) are then converted into approximate velocity fields in the east and up displacement components, which we refer to as near-east and near-up velocity fields (Figure S9 in Supporting Information S1; Drouin & Sigmundsson, 2019). The near-east velocity field is relative to a fixed Eurasian plate. Both the near-east and near-up velocity fields are in good agreement with GNSS velocities (Figure S10 in Supporting Information S1).

The near-east velocity field (Figure S9d in Supporting Information S1) suggests a transition from westward movement to eastward movement when going from the west to the east. Plate spreading in the area produces 18–19 mm/yr displacement in this region in the N(100–105)°E direction, which is the main reason for the horizontal divergent movement in the near-east velocity field. The vertical decomposed InSAR velocity field (Figure

S9e in Supporting Information S1) shows uplift in the whole study area, which is under the influence of GIA. These extra deformation processes are corrected in the average velocity fields using the same procedure as for the GNSS data.

2.3. Velocities Corrected for GIA and Plate Spreading

After removal of models for GIA and plate spreading from the observations, the remaining GNSS and InSAR velocity field (Figures 3a and 3e), which we refer to as corrected velocities, show spatially coherent motion centered on the dike. The near-east corrected velocity field (Figure 3a) shows displacements away from the dike, slightly higher on the west side of the dike than on the east side. The horizontal movement is largest about 11 km away from the dike. In the vertical direction, the area is uplifting, with the maximum uplift observed at the edge of the ice cap (Figure 3e). An uplift rate higher than 10 mm/yr occupies a larger area on the east side than on the west side of the dike. The profile across the dike suggests both broad long-wavelength deformation and focused, near-dike, short-wavelength deformation along the dike (Figures 3d and 3h). An InSAR near-east displacement profile of selected points near the dike suggests temporal variation in the near-field of the dike (Figure S11 in Supporting Information S1). Both the horizontal and vertical velocity fields have localized signals in the area directly above the dike and where the eruption occurred.

3. Modeling and Results

To test the hypothesis that viscoelastic relaxation is the main source of the post-rifting deformation signal, we employ a suite of viscoelastic models by varying elastic plate thickness and viscosity parameters, in order to simulate post-rifting relaxation induced surface displacement following the Bárðarbunga-Holuhraun dike intrusion.

We use the semi-analytical software RELAX (Barbot & Fialko, 2010a, 2010b) to calculate post-rifting displacement fields in response to the formation of a dike. We start with a two-layer Maxwell viscoelastic model, where a 7 km thick elastic layer lies on top of a 0.3×10^{19} Pa s viscoelastic half-space, as described by Li et al. (2021). Both layers consist of homogeneous isotropic material, with Poisson's ratio $\nu = 0.25$ and shear modulus $\mu = 16$ GPa (Grapenthin et al., 2006). The dike model is inferred from co-eruptive deformation by Sigmundsson et al. (2015). The injected dike is divided into 120 patches down to 10 km depth. Each patch is 2 km deep, with the opening in the range of 0.09–8.87 m. The average opening of the patches is 1.0 m, with the majority of the opening occurring above 6 km depth.

We determine the RMS of the model residuals and expect that the parameter combinations that yield the smallest RMS fit our observation best (Figures 4 and S12 in Supporting Information S1). By giving different weights to GNSS and InSAR average velocity fields, as well as horizontal and vertical components, we can combine all average displacement fields to determine the model that best explains our observations. GNSS and InSAR average velocities are used with a relative weight of 1000:1 (See details in Figure S13 in Supporting Information S1). As the horizontal velocities are less influenced by seasonal variations than the vertical components (e.g., Figure 2), the horizontal velocity is given twice the weight of the vertical velocity.

The difference between observed velocities and those predicted by the starting model yields residuals with a larger RMS (9.0 mm/yr) than if a zero model is applied (4.1 mm/yr). Therefore, we consider a range of different elastic layer thicknesses and viscosities to explain the corrected velocities. We explore elastic layer thickness ranging from 1 to 24 km in steps of 1 km. As the displacement rate predicted by the viscoelastic model scales inversely with viscosity, we derive the result of different viscosities by scaling the displacement rate of the initial model, as done by Li et al. (2021). We test viscosities in 0.1×10^{19} Pa s steps from 0.3 – 3.6×10^{19} Pa s.

Our residual analysis produces an RMS misfit space that contains two areas of good fit (Figure 4), one centered at a 2 km thick elastic layer and 1.2×10^{19} Pa s, while the other is at 18 km and 0.4×10^{19} Pa s. This nonconvex misfit space represents model sensitivities to near-dike, short-wavelength deformation (2 km thick and 1.2×10^{19} Pa s) and broad long-wavelength deformation (18 km, 0.4×10^{19} Pa s) as captured in horizontal and vertical velocity fields (Figures S12 and S14 in Supporting Information S1). As post-eruptive deformation is generally a broad signal, we select 18 km and 0.4×10^{19} Pa s as the optimal model, which is also supported by the slightly lower

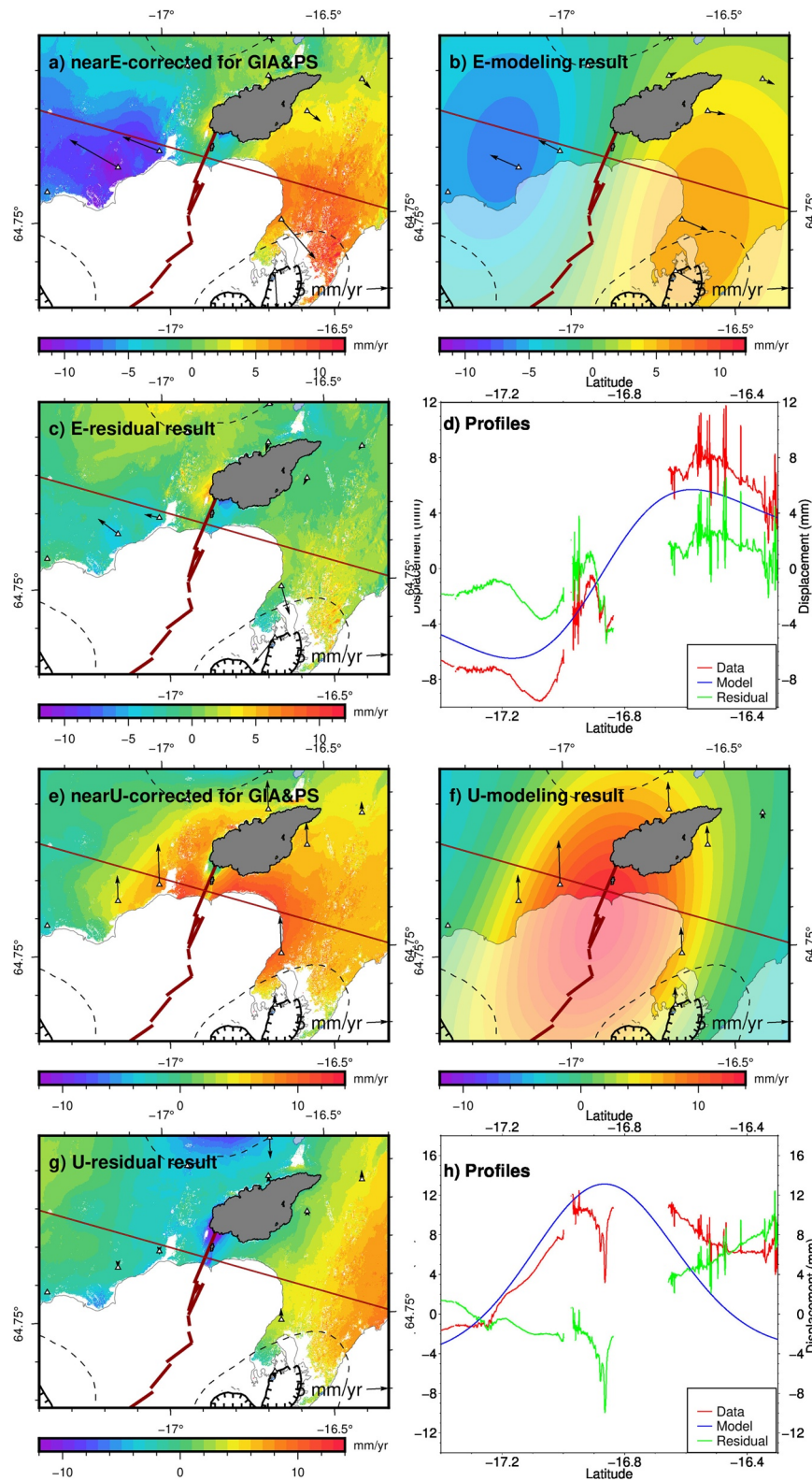


Figure 3. Corrected average velocity field in the (a–d) horizontal and (e–h) vertical directions during 2015–2020 from Interferometric Synthetic Aperture Radar (InSAR; color) and Global Navigation Satellite System (black arrows). The decomposed near-east and near-up InSAR average velocities after correcting glacial isostatic adjustment and plate spreading signals are in panels (a and e). The modeled east and up velocity from the viscoelastic model with the optimal elastic layer thickness (18 km) and viscosity (0.4×10^{19} Pa s) are in panels (b and f). Panels (c and g) are the differences between corresponding observations (a and e) and model (b and f). Panels (d and h) are the near-east (red line in panels (a, b, and c)) and near-up (red line in panels (e, f, and g)) velocity profiles across the study area.

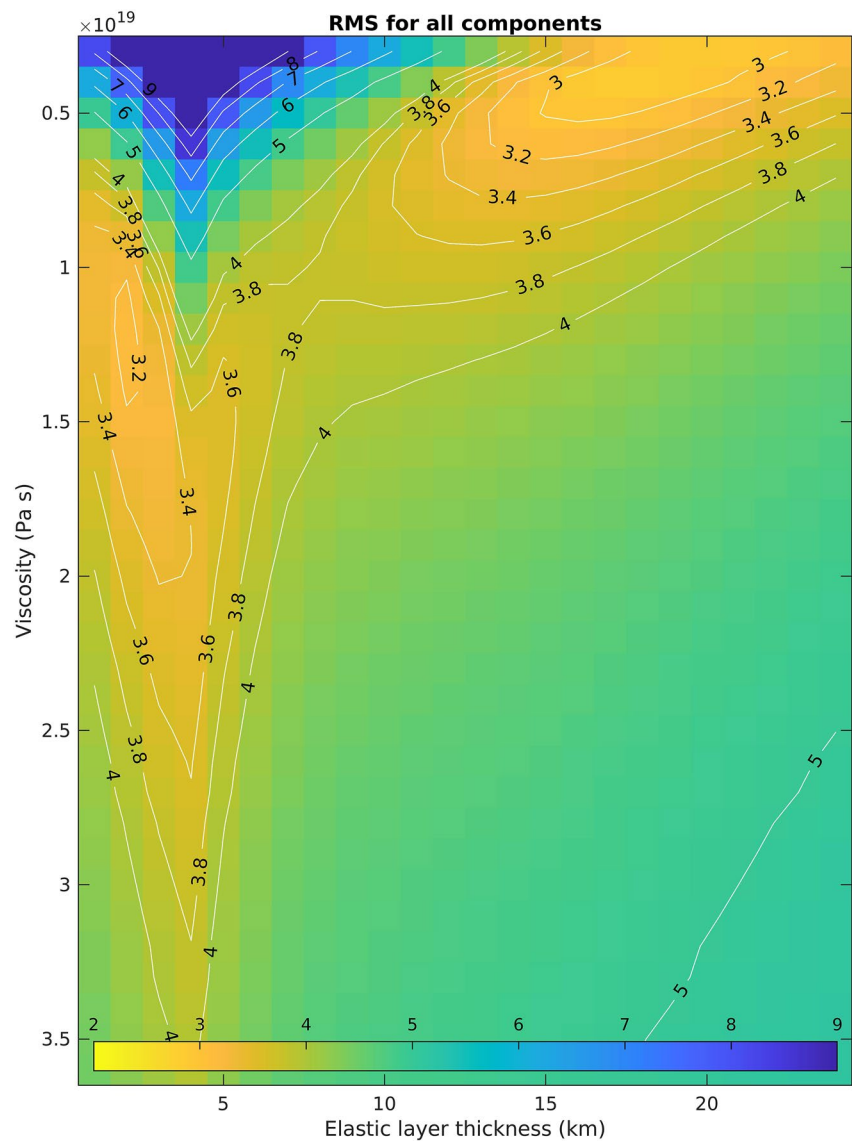


Figure 4. Root mean square residual between the corrected velocity fields (data) and modeling results. The data include near-east and near-up components from Interferometric Synthetic Aperture Radar (InSAR) and north, east, and up components from Global Navigation Satellite System (GNSS). The weight of GNSS versus InSAR is 1000:1. The weight of horizontal versus vertical is 2:1. The x-axis is the elastic layer thickness (1–24 km with 1 km step) and the y-axis is the viscosity ($0.3\text{--}3.6 \times 10^{19}$ Pa s with 0.1×10^{19} Pa s step). The optimal viscosity for the velocities is found at 0.4×10^{19} Pa s and the optimal elastic layer thickness is 18 km.

RMS residuals in that region of the parameter space. For the optimal model, the overall weighted RMS residual is improved from 4.1 for no model to 2.8 mm/yr. The RMS of the corrected velocity without a model is 5.5 and 5.2 mm/yr for InSAR near-east and near-up components, which improved to 1.8 and 3.9 mm/yr after removing the optimal viscoelastic model. The GNSS velocities are also improved from 5.6 (east), 5.5 (north), and 5.9 (up) mm/yr for no model to 2.8, 3.5, and 2.2 mm/yr, respectively.

Predicted displacements according to the model are compared to the corrected velocities from InSAR and GNSS in Figure 3. The near-east displacement rate on the west side of the dike is higher than on the east side of the dike (Figure 3b). The majority of the misfit in both the near-east and near-up velocity fields are in the close vicinity of the dike (Figures 3c and 3g). The near-up velocity field also shows misfit on the east side of the dike.

4. Discussion

The misfit space in Figure 4 shows two regimes that provide a good fit to our corrected velocity field based on the weighted RMS residual, one with an 18 km thick elastic layer and a viscosity of 0.4×10^{19} Pa s, the other with the localized minimum with elastic layer thickness at 2 km and viscosity at 1.2×10^{19} Pa s (Figure S15 in Supporting Information S1). These two regimes correspond well to the different preferred models by the horizontal and vertical velocity fields (Figure S14 in Supporting Information S1). The horizontal velocity field prefers a model with a thinner elastic layer (3 km) and higher viscosity (1.5×10^{19} Pa s, Figure S16 in Supporting Information S1), while the vertical velocity field prefers a model with a thicker elastic layer (24 km) and lower viscosity (0.4×10^{19} Pa s, Figure S17 in Supporting Information S1). Nevertheless, all models suggest the viscosity in the region is in the range of $0.4\text{--}1.5 \times 10^{19}$ Pa s.

To explain the different preferred elastic layer thicknesses for the horizontal and vertical velocity fields, we propose possibilities such as inappropriate GIA modeling, higher ice mass-loss rate in the area, or renewed magma inflow. Our test suggests that applying a different GIA scaling factor to the model by Auriac (2014) can not explain the excess uplift (Figure S18 in Supporting Information S1). The higher ice mass-loss rate in recent years at Vatnajökull (Compton et al., 2015) might explain the excess uplift. However, more detailed ice loss data is needed to quantify the produced deformation field. The trend change in the east component of KVEC timeseries in 2017 (Figure 2) might suggest magma injected into the dike, as observed at Ghoubbet-Asal (Cattin et al., 2005). A similar mismatch between horizontal and vertical viscoelastic post-rifting model fit is found by Nooner et al. (2009) in Afar.

We select our preferred model, 18 km and 0.4×10^{19} Pa s, based on an overall lower misfit and the reasoning that viscoelastic processes are generally of longer spatial wavelength. However, this model does not explain the localized deformation residual directly above the dike in the corrected InSAR average velocity fields (Figures 3a and 3e). The horizontal motion toward the dike and subsidence above the dike could be a result of non-linear displacement in this area, as suggested by the InSAR timeseries (Figure S11 in Supporting Information S1). The co-eruptive model has the largest dike opening, 8.87 m, in this area. The cooling of the dike, resulting in localized contraction, could be the explanation for this localized signal. Non-homogeneous subsurface structure close to the dike, or an over-estimation of the opening from the co-eruptive model could provide alternate explanations.

Compared with previous GIA studies at Vatnajökull, which suggest an elastic crustal thickness in the range of 10–40 km and the viscosity of the shallow mantle at $0.1\text{--}1 \times 10^{19}$ Pa s (Auriac, 2014; Árnadóttir et al., 2009; Fleming et al., 2007; Pagli et al., 2007), our model suggests a comparable elastic layer thickness and viscosity. The viscosity underneath Bárðarbunga caldera, around 30 km away from our study area, was estimated to be 0.3×10^{19} Pa s (Li et al., 2021), which is comparable to the value found here.

The approximately 1.4 km^3 Holuhraun lava field formed in 2014–2015 over an 84 km^2 area (Pedersen et al., 2017). To understand whether the response to loading by the lava field influences our deformation field, we run a forward model considering the lava load in a $7 \times 17 \text{ km}$ rectangular area with uniform lava thickness of 17 m and density of 2300 kg/m^3 , using the same subsurface structure as in our optimal model. This yields an insignificant viscoelastic response at the edges of the Holuhraun lava field of less than 1 mm/yr in the horizontal component and less than 4 mm/yr in the vertical direction during our study period.

Our study considers a two-layer viscoelastic model with homogeneous isotropic Maxwell material to explain average velocities and the spatial pattern of deformation. We pay less attention to the temporal variation measured at GNSS stations in the area, which could be further explored in future studies. More complex model geometries, such as the model with three or more layers, with non-linear rheology, or considering lateral variation in layer thickness and viscosity, could be considered in future studies, to better understand the subsurface structure of our area.

5. Conclusion

We analyze the post-rifting ground deformation field around the Bárðarbunga-Holuhraun dike. After correcting for the background deformation field (GIA and plate spreading signal), the remaining signal shows horizontal displacement away from the dike and uplift. Our modeling result suggests that a two-layer viscoelastic model considering an elastic layer on top of a viscoelastic half-space can explain both the horizontal and vertical

deformation signal. The optimal model that best explains the displacement fields has 0.4×10^{19} Pa s viscoelastic material below an 18 km thick elastic layer. Another alternate parameter combination consists of an elastic layer thickness of 2 km and viscosity of 1.2×10^{19} Pa s, which is likely due to unmodeled short wavelength signals in the vicinity of the dike. Our study suggests that viscoelastic relaxation is an important process to consider after a rifting event. Alternate modeling approaches to that considered here or other processes such as cooling of the dike, ongoing dike inflation, and - in the case of Iceland - time-varying GIA, heterogeneous viscosity and elastic layer thickness may have to be invoked to fully explain the deformation field.

Data Availability Statement

Interferometric Synthetic Aperture Radar average velocity field is available at <https://doi.org/10.17605/OSF.IO/3B2GF>. SAR images from Sentinel-1 satellites are retrieved from Copernicus Open Access Hub (<https://scihub.copernicus.eu/dhus/#/home>) provided by European Space Agency. Rinex data for calculating the GNSS timeseries are available at UNAVCO Inc. uploaded by Grapenthin (2016a, 2016b, 2016c, 2016d, 2016e) (<https://doi.org/10.7283/WKZ3-NW79>, <https://doi.org/10.7283/QSTY-N037>, <https://doi.org/10.7283/PDN2-N051>, <https://doi.org/10.7283/N65C-JN46>, <https://doi.org/10.7283/XN8V-RZ54>). RELAX software used for viscoelastic deformation modeling is available at <https://github.com/geodynamics/relax>. The dike model is published by Sigmundsson et al. (2015). Details of the Iceland map is provided by Sigmundsson et al. (2020). Holuhraun lava field contour is described in Pedersen et al. (2017). MATLAB (2020) is used for calculation and figure plotting, and some figures are plotted by the Generic Mapping Tools (Wessel et al., 2013).

Acknowledgments

We thank the Research Fund of the University of Iceland for funding for the Ph.D. work of the first author (S. Li), of which this research is a part of. Partial financial support from the H2020 project EUROVOLC funded by the European Commission is acknowledged (Grant No. 731070). R. Grapenthin acknowledges partial support for this work through NSF grant EAR-1464546. We thank Chiara Lanzi for helping to benchmark the dike model. We thank the fruitful discussion with Halldór Geirsson and Andrew Hooper. We thank the reviewer for the constructive comments, which helped strengthen our manuscript. We thank the editor and editor's assistant for their time in helping us with this article.

References

- Ágústssdóttir, T., Winder, T., Woods, J., White, R. S., Greenfield, T., & Brandsdóttir, B. (2019). Intense seismicity during the 2014–2015 Bárðarbunga–Höluhraun rifting event, Iceland, reveals the nature of dike-induced earthquakes and caldera collapse mechanisms. *Journal of Geophysical Research: Solid Earth*, 124(8), 8331–8357. <https://doi.org/10.1029/2018JB016010>
- Ágústssdóttir, T., Woods, J., Greenfield, T., Green, R. G., White, R. S., Winder, T., et al. (2016). Strike-slip faulting during the 2014 Bárðarbunga–Höluhraun dike intrusion, central Iceland. *Geophysical Research Letters*, 43(4), 1495–1503. <https://doi.org/10.1002/2015GL067423>
- Árnadóttir, T., Lund, B., Jiang, W., Geirsson, H., Björnsson, H., Einarsson, P., & Sigurdsson, T. (2009). Glacial rebound and plate spreading: Results from the first countrywide GPS observations in Iceland. *Geophysical Journal International*, 177(2), 691–716. <https://doi.org/10.1111/j.1365-246X.2008.04059.x>
- Ali, S. T., Feigl, K. L., Carr, B. B., Masterlark, T., & Sigmundsson, F. (2014). Geodetic measurements and numerical models of rifting in Northern Iceland for 1993–2008. *Geophysical Journal International*, 196(3), 1267–1280. <https://doi.org/10.1093/gji/ggt462>
- Altamimi, Z., Rebischung, P., Métivier, L., & Collilieux, X. (2016). ITRF2014: A new release of the International Terrestrial Reference Frame modeling nonlinear station motions. *Journal of Geophysical Research: Solid Earth*, 121(8), 6109–6131. <https://doi.org/10.1002/2016JB013098>
- Argus, D. F., Gordon, R. G., Heflin, M. B., Ma, C., Eanes, R. J., Willis, P., et al. (2010). The angular velocities of the plates and the velocity of Earth's centre from space geodesy. *Geophysical Journal International*, 180(3), 913–960. <https://doi.org/10.1111/j.1365-246X.2009.04463.x>
- Auriac, A. (2014). *Solid earth response to ice retreat and glacial surges in Iceland inferred from satellite radar interferometry and finite element modelling*. Doctoral dissertation. Faculty of Earth Sciences, University of Iceland.
- Barbot, S., & Fialko, Y. (2010a). Fourier-domain Green's function for an elastic semi-infinite solid under gravity, with applications to earthquake and volcano deformation: Fourier-domain elastic solutions. *Geophysical Journal International*, 182(2), 568–582. <https://doi.org/10.1111/j.1365-246X.2010.04655.x>
- Barbot, S., & Fialko, Y. (2010b). A unified continuum representation of post-seismic relaxation mechanisms: Semi-analytic models of after-slip, poroelastic rebound and viscoelastic flow: Semi-analytic models of postseismic transient. *Geophysical Journal International*, 182(3), 1124–1140. <https://doi.org/10.1111/j.1365-246X.2010.04678.x>
- Cattin, R., Doubre, C., De Chabalière, J.-B., King, G., Vigny, C., Avouac, J.-P., & Ruegg, J.-C. (2005). Numerical modelling of quaternary deformation and post-rifting displacement in the Asal–Ghoubbet rift (Djibouti, Africa). *Earth and Planetary Science Letters*, 239(3–4), 352–367. <https://doi.org/10.1016/j.epsl.2005.07.028>
- Compton, K., Bennett, R. A., & Hreinsdóttir, S. (2015). Climate-driven vertical acceleration of Icelandic crust measured by continuous GPS geodesy. *Geophysical Research Letters*, 42(3), 743–750. <https://doi.org/10.1002/2014GL062446>
- Drouin, V., & Sigmundsson, F. (2019). Countrywide observations of plate spreading and glacial isostatic adjustment in Iceland inferred by Sentinel-1 radar interferometry, 2015–2018. *Geophysical Research Letters*, 46(14), 8046–8055. <https://doi.org/10.1029/2019GL082629>
- Fleming, K., Martinec, Z., & Wolf, D. (2007). Glacial-isostatic adjustment and the viscosity structure underlying the Vatnajökull Ice Cap, Iceland. *Pure and Applied Geophysics*, 164(4), 751–768. <https://doi.org/10.1007/s00024-007-0187-6>
- Foulger, G. R., Jahn, C.-H., Seebur, G., Einarsson, P., Julian, B. R., & Heki, K. (1992). Post-rifting stress relaxation at the divergent plate boundary in Northeast Iceland. *Nature*, 358(6386), 488–490. <https://doi.org/10.1038/358488a0>
- Grapenthin, R. (2016a). Hopnet GPS network - GIGO-gigoldur p.s., the gage facility operated by UNAVCO, Inc., GPS/GNSS observations dataset [dataset]. UNAVCO, Inc. <https://doi.org/10.7283/WKZ3-NW79>
- Grapenthin, R. (2016b). Hopnet GPS network - KVEC-Kverkfjöll p.s., the gage facility operated by UNAVCO, Inc., GPS/GNSS observations dataset [dataset]. UNAVCO, Inc. <https://doi.org/10.7283/xn8v-rz54>
- Grapenthin, R. (2016c). Hopnet GPS network - LANH-Langahli p.s., the gage facility operated by UNAVCO, Inc., GPS/GNSS observations dataset [dataset]. UNAVCO, Inc. <https://doi.org/10.7283/N65C-JN46>
- Grapenthin, R. (2016d). Hopnet GPS network - MOFC-Moflatir p.s., the gage facility operated by UNAVCO, Inc., GPS/GNSS observations dataset [dataset]. UNAVCO, Inc. <https://doi.org/10.7283/PDN2-N051>

- Grapenthin, R. (2016e). Hopnet GPS network - RIFC-Rifnihnjukur, the gage facility operated by UNAVCO, Inc., GPS/GNSS observations dataset [dataset]. UNAVCO, Inc. <https://doi.org/10.7283/QSTY-N037>
- Grapenthin, R., Sigmundsson, F., Geirsson, H., Árnadóttir, T., & Pinel, V. (2006). Icelandic rhythmicity: Annual modulation of land elevation and plate spreading by snow load. *Geophysical Research Letters*, 33(24), L24305. <https://doi.org/10.1029/2006GL028081>
- Gudmundsson, M. T., Jónsdóttir, K., Hooper, A., Holohan, E. P., Halldórsson, S. A., Ófeigsson, B. G., et al. (2016). Gradual caldera collapse at Bárðarbunga volcano, Iceland, regulated by lateral magma outflow. *Science*, 353(6296), aaf8988. <https://doi.org/10.1126/science.aaf8988>
- Hamling, I. J., Wright, T. J., Calais, E., Lewi, E., & Fukahata, Y. (2014). InSAR observations of post-rifting deformation around the Dabbahu rift segment, Afar, Ethiopia. *Geophysical Journal International*, 197(1), 33–49. <https://doi.org/10.1093/gji/ggu003>
- Herring, T., King, R., & McClusky, S. (2010). *Introduction to GAMIT/GLOBK*. Massachusetts Institute of Technology.
- Hreinsdóttir, S., Árnadóttir, T., Decriem, J., Geirsson, H., Tryggvason, A., Bennett, R. A., & LaFemina, P. (2009). A complex earthquake sequence captured by the continuous GPS network in SW Iceland. *Geophysical Research Letters*, 36(12), L12309. <https://doi.org/10.1029/2009GL038391>
- Jacoby, W. R., Hartmann, O., Wallner, H., Smilde, P. L., Buerger, S., Sjöberg, L. E., et al. (2009). Temporal gravity variations near shrinking Vatnajökull ice cap, Iceland. *Pure and Applied Geophysics*, 166(8), 1283–1302. <https://doi.org/10.1007/s00024-009-0499-9>
- Li, S., Sigmundsson, F., Drouin, V., Parks, M. M., Ófeigsson, B. G., Jónsdóttir, K., et al. (2021). Ground deformation after a caldera collapse: Contributions of magma inflow and viscoelastic response to the 2015–2018 deformation field around Bárðarbunga, Iceland. *Journal of Geophysical Research: Solid Earth*, 126(3), e2020JB020157. <https://doi.org/10.1029/2020JB020157>
- MATLAB. (2020). *Version 9.8.0.1323502 (r2020a)*. The MathWorks Inc. Retrieved from <https://www.mathworks.com/products/matlab.html>
- Nooner, S. L., Bennati, L., Calais, E., Buck, W. R., Hamling, I. J., Wright, T. J., & Lewi, E. (2009). Post-rifting relaxation in the Afar region, Ethiopia. *Geophysical Research Letters*, 36(21), L21308. <https://doi.org/10.1029/2009GL040502>
- Pagli, C., Sigmundsson, F., Lund, B., Sturkell, E., Geirsson, H., Einarsson, P., et al. (2007). Glacio-isostatic deformation around the Vatnajökull ice cap, Iceland, induced by recent climate warming: GPS observations and finite element modeling. *Journal of Geophysical Research*, 112(8), 1–12. <https://doi.org/10.1029/2006JB004421>
- Parks, M. M., Heimgsson, E. R., Sigmundsson, F., Hooper, A., Vogfjörð, K. S., Árnadóttir, T., et al. (2017). Evolution of deformation and stress changes during the caldera collapse and dyking at Bárðarbunga, 2014–2015: Implication for triggering of seismicity at nearby Tungnafellsjökull volcano. *Earth and Planetary Science Letters*, 462, 212–223. <https://doi.org/10.1016/j.epsl.2017.01.020>
- Pedersen, G., Höskuldsson, A., Dürig, T., Thordarson, T., Jónsdóttir, I., Riisshuus, M., et al. (2017). Lava field evolution and emplacement dynamics of the 2014–2015 basaltic fissure eruption at Holuhraun, Iceland. *Journal of Volcanology and Geothermal Research*, 340, 155–169. <https://doi.org/10.1016/j.jvolgeores.2017.02.027>
- Pollitz, F. F., & Sacks, I. S. (1996). Viscosity structure beneath northeast Iceland. *Journal of Geophysical Research*, 101(B8), 17771–17793. <https://doi.org/10.1029/96JB01074>
- Rosen, P. A., Gurrola, E., Sacco, G. F., & Zebker, H. (2012). The InSAR scientific computing environment. In *Eusar 2012; 9th european conference on synthetic aperture radar* (pp. 730–733). VDE.
- Sigmundsson, F., Einarsson, P., Hjartardóttir, Á. R., Drouin, V., Jónsdóttir, K., Árnadóttir, T., et al. (2020). Geodynamics of Iceland and the signatures of plate spreading. *Journal of Volcanology and Geothermal Research*, 391, 106436. <https://doi.org/10.1016/j.jvolgeores.2018.08.014>
- Sigmundsson, F., Hooper, A., Hreinsdóttir, S., Vogfjörð, K. S., Ófeigsson, B. G., Heimgsson, E. R., et al. (2015). Segmented lateral dyke growth in a rifting event at Bárðarbunga volcanic system, Iceland. *Nature*, 517(7533), 191–195. <https://doi.org/10.1038/nature14111>
- Wessel, P., Smith, W. H. F., Scharroo, R., Luis, J., & Wobbe, F. (2013). Generic mapping tools: Improved version released. *Eos, Transactions American Geophysical Union*, 94(45), 409–410. <https://doi.org/10.1002/2013EO450001>
- Woods, J., Donaldson, C., White, R. S., Caudron, C., Brandsdóttir, B., Hudson, T. S., & Ágústssdóttir, T. (2018). Long-period seismicity reveals magma pathways above a laterally propagating dyke during the 2014–15 Bárðarbunga rifting event, Iceland. *Earth and Planetary Science Letters*, 490, 216–229. <https://doi.org/10.1016/j.epsl.2018.03.020>
- Wright, T. J., Sigmundsson, F., Pagli, C., Belachew, M., Hamling, I. J., Brandsdóttir, B., et al. (2012). Geophysical constraints on the dynamics of spreading centres from rifting episodes on land. *Nature Geoscience*, 5(4), 242–250. <https://doi.org/10.1038/ngeo1428>